

Critical Role of Processing on the Mechanical Properties of Cross-Linked Highly Loaded Nanocomposites

Karthika Suresh,^{†,‡} Arindam Chowdhury,[§] Sanat K. Kumar,^{*,||} and Guruswamy Kumaraswamy^{*,†,‡}

[†]J-101, Polymers and Advanced Materials Laboratory, Complex Fluids and Polymer Engineering, Polymer Science and Engineering Division, CSIR-National Chemical Laboratory, Pune 411008, Maharashtra, India

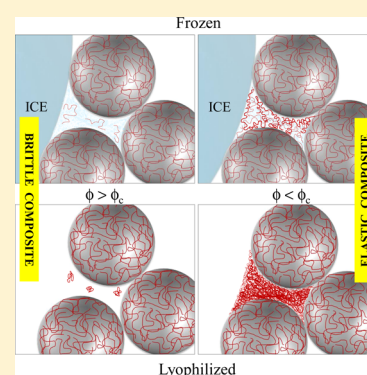
[‡]Academy of Scientific and Innovative Research, (AcSIR), New Delhi 110 025, India

[§]Department of Chemistry, Indian Institute of Technology Bombay, Powai, Mumbai 400076, Maharashtra, India

^{||}Department of Chemical Engineering, Columbia University, New York, New York 10027, United States

S Supporting Information

ABSTRACT: Polymer nanocomposites are frequently not at equilibrium—therefore, the structure and properties critically depend on the protocol followed in their preparation. Here, we demonstrate that the elastic–brittle transition in highly loaded ice-templated polymer nanocomposites is sensitively determined by the conformation of polymer chains during nanocomposite preparation. Macroporous polymer nanocomposites are synthesized using two preparation pathways, both exhibiting minor modifications of the ice-templating method wherein an aqueous dispersion of nanoparticles, polymers, and cross-linkers is frozen. In one method, the matrix polymer is cross-linked in the presence of ice, whereas in the other method, the ice is removed by freeze-drying before the polymer is cross-linked. Although all measurable structural metrics are practically identical for the two composites, they exhibit qualitatively different mechanical properties. Nanocomposites cross-linked in the presence of ice show exceptional resilience, recovering elastically from large compression for very high nanoparticle loadings—in some instances, above 90% by weight. Here, the critical particle loading for the elastic–brittle transition is dependent on the molecular weight of the polymer. In comparison, samples cross-linked after freeze-drying appear structurally identical but turn brittle at much lower particle loadings (about 60% by weight), independent of the matrix polymer molecular weight. We rationalize these differences in terms of the conformational state of the polymer during cross-linking. In the former case, polymer chains are in good solvent during nanocomposite preparation, while after lyophilization, they are in a poor solvent. The large spatial extent of well-solvated chains and chain–chain overlap during cross-linking results in the formation of intermolecular cross-links, and we obtain elastic nanocomposites even at high nanoparticle loadings. In contrast, for chains in collapsed conformations in a bad solvent, chain connectivity during cross-linking is achieved only for much lower particle loadings. Our results reiterate that the sensitivity of polymer conformations to different processing methods can result in large differences in properties, even though their consequences on structural characteristics are effectively indistinguishable.



INTRODUCTION

Polymer nanocomposites are of great current interest because they combine the flexibility of polymers with the functionality and rigidity of inorganic nanofillers.^{1–11} It is commonly believed that adding progressively smaller nanoparticles (NPs), which leads to increased surface-to-volume ratios, is beneficial from a property standpoint. However, a critical variable in this context is the NP spatial dispersion in the polymer—because particle agglomeration tends to reduce the surface area available for interactions with the polymer, which reduces the potential advantages of using nanometer-sized particles. Two dominant themes have now emerged to address these issues. First, the grafting of chains onto the NP surfaces, to create polymer-grafted nanoparticles, has proven to be a facile means of controlling NP dispersion.^{12–15} Second, it has

become increasingly clear that the solvent used to formulate nanocomposites of bare NPs with polymers can (and frequently does) dramatically alter the state of dispersion through the modification of the effective (solvent-mediated) interactions between the NPs and the polymer.¹⁶

Although these ideas have led to a great deal of effort in the community, the primary focus of these efforts is in the context of dilute NPs, that is, systems where the polymer is the dominant component. Inspired by biology, however, there continues to be interest in nanocomposites in the opposite limit of dilute polymer. A good example of such an inspiration

Received: April 20, 2019

Revised: June 21, 2019

Published: July 31, 2019

is Nacre, which is $\approx 95\%$ inorganic (namely platelike aragonite) mixed with a small amount of biopolymer adhesive.^{17–19} Although Nacre exhibits exceptional toughness, typically such materials fail when deformed to relatively low strains. Some time ago, we reported the creation of ice-templated hybrid materials that recover elastically from large compressive stress.²⁰ Ice templating is a versatile method that has been employed for processing nanomaterials and polymers to form porous objects. Materials with functional properties have been prepared using ice templating for use in applications ranging from biomedical scaffolds, microfluidics, molecular filtration, organoelectronics, photovoltaics, and fuel cells.^{21–30} The modified ice-templating procedure we used is simple: a mixture of particles, polymer, cross-linker, and water is mixed and then frozen. The ice, which presumably excludes all impurities, yields an interconnected nanoparticle structure (with strut sizes in the 100 μm size range) where the NPs (we use particles ranging in size from 20 nm to 1 μm) are interconnected by a thin cross-linked polymer mesh. Remarkably, the mechanical response is qualitatively independent of particle size and chemistry and we have demonstrated this for different particles, polymers, and cross-linking chemistries.²⁰

However, the protocol for creating these composites is important.³¹ In one case, we allow the (slow) cross-linking reaction to occur in the presence of ice crystals, whereas in the second case, we remove the ice rapidly through the process of lyophilization before cross-linking the polymer. We have shown that changing the protocol leads to materials that look structurally identical (*viz.*, have the very similar pore structure, interparticle spacing, and monolith connectivity; the same polymer content and polymer/cross-linker ratio; as well as average degree of cross-linking^{31,32}) but have qualitatively different local NP dynamics.³³ Here, we go beyond these fundamental insights and examine how these different preparation protocols result in microstructural differences that underpin macroscopic mechanical properties, in particular the response of nanocomposite monoliths to compression and their subsequent recovery.

MATERIALS AND METHODS

Materials. LUDOX-TM silica particles (manufacturer-specified size = 22 nm) are obtained as a 50% (w/v) dispersion. Silica particles (1 μm) were obtained from Richen Industries (Hong Kong). Polystyrene spherical monodisperse (1.08 \pm 0.04 μm) fluorescent particles (PS-FluoGreen-1.0, ab/em: 492/519 nm, 2.5 wt %) were purchased from microParticles GmbH (Germany). Branched polyethylenimines of weight-average molecular weights 0.8 kDa (M_n = 0.6 kDa), 25 kDa (M_n = 10 kDa), and 750 kDa (M_n = 60 kDa) and 1,4-butanediol diglycidyl ether were obtained from Sigma-Aldrich (molecular weights as specified by the supplier). All materials were used as received. Glass coverslips for the epifluorescence microscopy were purchased from Corning (No. 1), USA.

Sample Preparation. Briefly, samples were prepared by ice-templating an aqueous dispersion of silica particles (either 22 nm diameter LUDOX nanoparticles or 1 μm diameter silica particles), polyethylenimine (molecular weights, M_w = 0.8, 25, and 750 kDa), and a diepoxy cross-linker. We observe a qualitatively similar behavior for samples prepared using 22 nm and 1 μm silica particles. We systematically vary the inorganic content of the samples from ϕ = 0% (no silica nanoparticles) to 95% (by weight), while maintaining a constant ratio of polymer to cross-linker. Macroporous monolith samples were prepared by cross-linking the polymer to form a mesh that binds the particles. The detailed preparation protocol is given below.

Preparation of Composites with Varying Particle Contents.

Silica particles (60 mg, LUDOX TM or 1 μm silica particles) were dispersed in deionized (DI) water by sonicating for 30 min (Supporting Information, Figure S1). To this, 'X' mg of polyethylenimine (PEI) stock solution of 10 wt % concentration was added, followed by vortexing it for 10 min. 'Y' mg of cross-linker; 1,4 butane dioldiglycidyl ether was added to this dispersion and vortexed for 3 min. On the basis of this general protocol, we have prepared 14 different aqueous dispersions with different particle concentrations. The % particle contents relative to total solid contents in the composites were 95, 93, 91, 83, 80, 71, 67, 57, 50, 40, 20, 10, 5, and 0%. The overall solid [i.e., silica particles + organic (=polymer + cross-linker)] concentration in the aqueous dispersion was 10 wt % (obtained by adjusting the DI water content). In these compositions, the 'X' values were 1, 1.5, 2, 4, 5, 8, 10, 15, 20, 30, 80, 180, 380, and 60 mg, respectively. PEI to cross-linker ratio was fixed at 1:2. We prepared composites in two different ways using these aqueous dispersions: (i) dispersions were kept at -18°C for 24 h followed by drying of the composites for 10 h using a lyophilizer (Labconco FreeZone 2.5 Plus, -80°C , 0.1 mBar). Here, the polymer/cross-linker reaction takes place in the frozen state, in the presence of ice crystals. (ii) In a second case, the dispersions were kept at -18°C for 45 min, followed by lyophilization at -80°C for 10 h. After lyophilization, the samples were transferred back to the freezer (-18°C) for 24 h. Here, the reaction between the polymer and the cross-linker takes place in the absence of ice crystals. The samples for the epifluorescence microscopy imaging were prepared by adding 58 mg of silica particles and 2 mg of fluorescent polystyrene (FPS) particles into the aqueous dispersion. This aqueous dispersion was used to prepare porous composites using the aforementioned protocol.

Characterization of Composites. We have characterized the materials which are cross-linked in the presence and absence of ice crystals using small-angle X-ray scattering (SAXS), rheometry, and epifluorescence microscopy.

Small-Angle X-ray Scattering. SAXS was performed on a Rigaku system. This instrument is equipped with a microfocussing rotating anode X-ray generator and a confocal max flux mirror, three pinhole collimators, and a two-dimensional detector (HyPix-3000). The detector is calibrated using a silver behenate standard. Experiments were performed at room temperature ($\sim 25^\circ\text{C}$). We performed SAXS on a dilute solution of LUDOX silica particles (2 wt %) filled in a capillary tube (diameter 2 mm; wall thickness $\approx 10 \mu\text{m}$). The data were circularly averaged, and the one-dimensional scattered intensity is presented after background subtraction, corrected for sample transmission. SAXS data were analyzed using SASFIT.³⁴

Rheometry. Compression/expansion studies on the composites were performed using an ARES G2 strain-controlled rheometer in a dynamic mechanical analysis measurement mode. Cylindrical samples were placed between two 25 mm diameter roughened parallel plates and 0.5 g of preload was applied. Samples were compressed to different strains at a constant rate of 0.1 mm/s and the corresponding normal force was measured. Nominal compression stress was calculated by dividing the compressive force with the initial cross-sectional area of the cylindrical sample. Experiments were repeated on minimum three fresh samples to confirm the reproducibility of the results. Representative data are presented in this work.

Single-Particle Tracking. A home-built epifluorescence microscope was used to image the fluorescent particles. The circular area of the sample was illuminated by focusing a circularly polarized 488 nm cw diode-pumped solid-state laser (Laserglow, 50 mW) onto the back focal plane of a 60X, 1.49 NA oil immersion objective (Nikon, Apo plan TIRF). The emitted light from the sample was collected by the same objective lens and passed through a dichroic mirror. The emitted light was impinged on a cooled (-25°C) interline CCD camera by guiding through a pinhole and a filter wheel. Time-lapse movies were captured for 10 min at 1 Hz frequency with a laser exposure time of 150 ms. Videos were collected using DVC View software. Background subtraction and smoothing of these image frames were done using ImageJ software (NIH). After the background subtraction, the FPS particles exhibit a signal-to-background ratio of

20–35. We have located the spatial positions of these particles over time using the centroid method.³⁵ This program was written in Matlab 7.8, and it gives the coordinates of the centroids of the bright particles. All the experiments were performed at 23 °C and 60% relative humidity using ambient temperature control system. All measurements were repeated multiple times to confirm their reproducibility.

Capillary Viscometer. Intrinsic viscosities of 0.8, 25, and 750 kDa PEIs were obtained by measuring the viscosities of polymer solutions using capillary viscometer (Schott Geräte). These viscometers were equipped with an optical system for flow detection. The temperature was maintained at 25 °C by a water bath. Polymer solutions with 0.5, 1, 2, 3, and 4 wt % concentrations are used for the measurements.

RESULTS

We shall show below that the mechanical properties of ice-templated porous nanocomposite monoliths change qualitatively, depending on the protocol employed in their preparation. To highlight this, we contrast the properties of “elastic” monoliths (prepared by freezing an aqueous dispersion of 1 μm silica particles and polymer, followed by cross-linking in the frozen state, see Experimental Section for details) with lyophilized monoliths (prepared by cross-linking after lyophilization of ice).

Mechanical Properties. We have previously shown³¹ that when ice-templated macroporous monoliths are prepared by first lyophilizing the ice crystal templates and then cross-linking the polymer, the resultant samples fail in a brittle manner on compression. For example, there is a near-linear increase in stress up to 5% strain when the $\phi = 91\%$ lyophilized monolith is compressed. Above this, there is an inflection in the stress–strain curve (at about 10% strain), and for further increase in strain, the stress increase is more gradual (Figure 1a). We

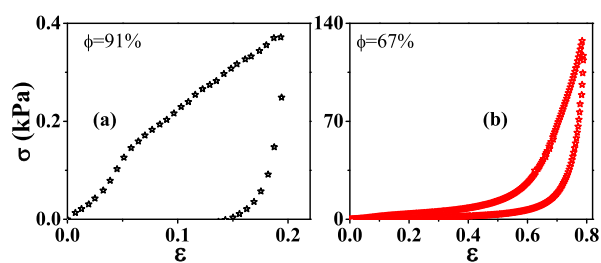


Figure 1. Compression/expansion properties of composites made from 1 μm silica and 25 kDa PEI and cross-linked in the absence of ice. Stress (σ)–strain (ϵ) curves of composites with ϕ (a) 91% and (b) 67% at 20% and 80% strains, respectively. Note the difference in σ and ϵ scales in (a,b).

associate the inflection in the stress–strain curve with the onset of brittle failure. X-ray microcomputed tomography indicates that for strains greater than the inflection, the pores collapse as their walls fail, resulting in monolith densification.³²

When we decrease strain after compressing the sample for strains exceeding 5%, the stress decreases abruptly to 0, indicating brittle failure of the monolith. A decrease in nanoparticle fraction, ϕ , results in an increase in strain for the onset of brittle failure and an increase in the stress borne by the monolith (Figures 1b, S2, and S3 in the Supporting Information). For example, for $\phi = 67\%$ (and lower, see the Supporting Information, Figures S2 and S3), there is a transition from brittle behavior, and the sample completely recovers after being compressed to strains as high as 80% (Figure 1b). Further, the stress required to compress these

monoliths to 80% strain is approximately 130 kPa, 2 orders of magnitude greater than the stress for the onset of brittle failure for the $\phi = 91\%$ monolith (compare Figures 1b and Supporting Information Figure S4).

In contrast to this behavior, macroporous monoliths with 91% solids prepared by cross-linking in the presence of ice recover their original size completely even after being subjected to compressive strains as large as 80% (Figures 2a). Only the samples with 93% solids (Figure 2b) show an

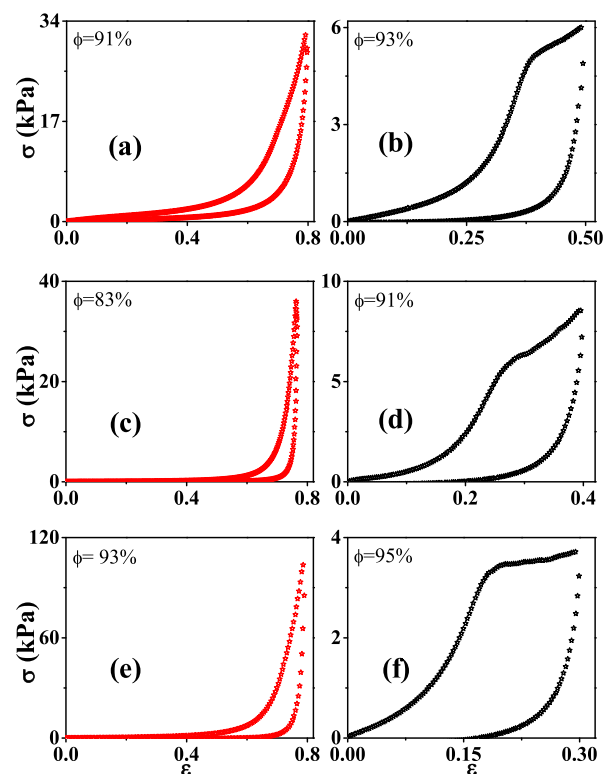


Figure 2. Compression/expansion data for composites prepared at different solid loadings (ϕ) of 1 μm silica, by cross-linking the polymer in the frozen state. The top row (a,b) shows data for samples prepared using PEI with $M_w = 25$ kDa, the middle row (c,d) for 0.8 kDa PEI, and the bottom row (e,f) for 750 kDa PEI. Note the difference in X and Y scales for each pair of samples.

inflection, indicating brittle failure. These results are sensitive to the molecular weight of the polymers under consideration—the solid concentration beyond which the brittle behavior occurs increases with increasing molecular weight of the polymer chains in question (Figure 2), that is, the polymer concentration corresponding to the brittle–ductile “transition” decreases with increasing chain molecular weight.

Thus, for both monoliths, lyophilized or cross-linked while frozen, there is a qualitative change in the mechanical response from elastic recovery to brittle failure, at a critical value of $\phi = \phi_c$. For lyophilized samples, this transition happens at $\phi_c \approx 57$ –67% for PEI with average molecular weights (M_w) varying from 0.8 to 750 kDa, independent of molecular weight (Figures 1 and Supporting Information Figures S2–S6). For samples cross-linked in the frozen state, this transition happens at a much higher ϕ and is polymer molecular-weight-dependent, viz., ϕ_c increases with increase in polymer molecular weight (Figures 2, Supporting Information Figures S7 and S8). We note that this qualitative transition in

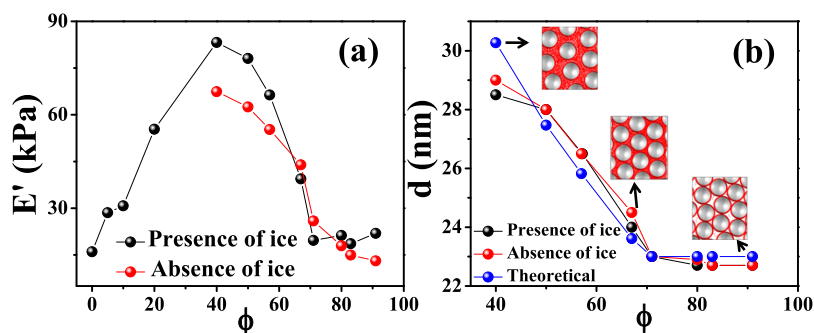


Figure 3. (a) Variation of Young's moduli of composites cross-linked in the presence and absence of ice as a function of filler loading, ϕ . (b) Variation of interparticle distance (measured as described in the section of NP structure) with particle concentration for samples cross-linked in the presence and absence of ice crystals along with theoretically calculated values.

mechanical response is observed for monoliths prepared using colloids varying in size from 22 nm to 1 μm and is, at best, weakly dependent on particle size (Supporting Information Figures S2–S8).

On compressing the monoliths, the stress increases monotonically. At low strains (<2%), the stress increases linearly with strain, allowing us to calculate Young's modulus as the slope of the stress–strain curve. Young's modulus of the macroporous monolith (frozen during cross-linking) increases monotonically with nanoparticle loading from $\phi = 0$ to 25% (Figure 3a). Surprisingly, increasing nanoparticle loading above $\phi = 40\%$ results in a decrease in the modulus of the composite monolith (Figure 3a). The modulus decreases monotonically until $\phi = 71\%$ and then plateaus between $\phi = 71$ and 91%, at a value comparable to the pure polymer modulus, independent of the presence of ice during cross-linking (Figure 3a). Thus, remarkably, the modulus of elastic monoliths is comparable to soft, pure polymeric foams even when loaded with 91% by weight of silica nanoparticles.

It is first important to emphasize that all of the effects we observe have their origins in the polymeric nature of the sample—the elastic modulus of silica, ≈ 70 GPa, is much higher than any of the numbers we report. The trends at low ϕ can be understood as being the “filler” effect as embodied in macroscopic theories such as the Guth–Gold model.³⁶ However, the nearly 3.5 times increase in the modulus on the addition of 40% filler is well beyond the predictions of the model. This result is unsurprising in light of our previous work,² where we concluded that this effect is a consequence of an interfacial polymer layer with properties intermediate between silica and the neat polymer. Here, we postulate the decrease in modulus beyond 40% solids to a decrease in the number of elastically active cross-links in the system. This effect, likely, has a two-fold origin. First, the increase in the particle volume fraction decreases the amount of polymer. To this point, a plot of E' as a function of $(1 - \phi)$ is found to be approximately linear, with an intercept corresponding to the pure polymer of ≈ 150 kPa. The rubber elasticity theory suggests that there should be $\approx 5 \times 10^{18}$ cross-links/ cm^3 which are elastically active. Since the modulus of the pure polymer, cross-linked under identical conditions, is about an order of magnitude smaller, we anticipate that this result reflects the reinforcing effect of the chains adsorbed on the NP surface. A second potential effect is that this decreased amount of polymer reduces the number of cross-links per unit volume of the polymer. We do not believe that this effect is important

except for concentrations above 71% filler. (More on this below.)

NP Structure. To understand the molecular origins of these mechanical results, we consider the structure of these hybrids. We used small-angle X-ray scattering, which is primarily sensitive to the scattering contrast between the silica and the other components in the system (water, polymer, and air), to deduce NP structuring. The experimentally accessible q -range in SAXS precludes characterization of composites containing 1 μm silica particles. Therefore, we present data on the nanocomposites containing 22 nm particles. We first obtain the NP form factor from dilute (2 wt %) silica dispersions. Fitting the dilute solution data yields a particle radius of 11 nm with a polydispersity parameter of 0.14 (Supporting Information Figure S9), consistent with a manufacturer-specified particle radius of 11 nm. Normalizing SAXS from the monoliths by the nanoparticle form factor yields an apparent structure factor, $S_A(q)$ (Supporting Information Figure S10). Since the particle concentration in the nanocomposite scaffold is not known, we note that $S_A(q)$ is scaled by an arbitrary constant. We obtain the average interparticle spacing by fitting the first peak in $S_A(q)$ with an interference function, given by $S_A(q) = A_2[1 + kg(q)]^{-1}$, where $g(q) = \frac{3 \sin qd - qd \cos qd}{q^3 d^3}$, A_2 is a constant, k is the packing factor, and d is the interparticle spacing.³⁷

The variation of the interparticle spacing, d , with the silica NP content, ϕ , deduced in this manner is similar for “elastic” and lyophilized monoliths (Figure 3b). d decreases approximately linearly from 29 nm at $\phi = 40\%$ to 23 nm at $\phi = 71\%$, beyond which we obtain a high- ϕ plateau value of d (≈ 23 nm). Scanning electron microscopy (SEM) images suggest that particles in the walls of the hybrid monolith are disordered (Supporting Information Figure S11). As the silica NPs are monomodal in size with modest polydispersity and are approximately spherical, we anticipate that they form a random close-packed structure, characterized by a packing fraction between 58 and 64%.³⁸ Assuming a silica density = 2.2 g/cc and PEI density in the adsorbed layer/melt phase = 1.05 g/cc, we calculate that there is insufficient cross-linked polymer to completely fill the void space between random close-packed silica particles in, for example, the $\phi = 91\%$ monolith. Between ϕ of 71 and 91%, the interparticle spacing is ≈ 23 nm, suggesting that the 22 nm silica particles are only separated by a thin layer of adsorbed polymer. The silica nanoparticles are negatively charged and cationic PEI forms an adsorbed monolayer on the particle surface in aqueous dispersion.^{39–41}

When the dispersion is ice-templated, the particles (decorated by this adsorbed layer) form a random close-packed structure in the monolith walls. Additional polymer that is not adsorbed is presumably localized to the interparticle voids. As the polymer content (relative to the particle) is increased starting from $\phi = 91\%$, viz., when ϕ is decreased, there is a critical value of ϕ when the interparticle voids are completely filled. For lower ϕ , the additional polymer increases the spacing between the nanoparticles. We calculate the interparticle spacing based on this simple geometric reasoning and observe remarkable agreement with the SAXS-determined NP spacing (Figure 3b).

Local NP Dynamics. We use single particle tracking microrheology to characterize the particle motion, which is a reflection of the local viscoelastic response of the cross-linked polymer mesh present in hydrated and lyophilized monoliths. We have previously reported that the use of wavelet transform-based filtering can eliminate drift from epifluorescence microscopy data, allowing one to track the motion of $1\ \mu\text{m}$ fluorescent probe particles in hybrid monoliths.³³ Using this technique, the thermal motion of NPs can be tracked with a resolution better than 3 nm. We prepared monoliths with ϕ varying from 50 to 91% using $1\ \mu\text{m}$ particles, with a small fraction of FPS latex particles, with 25 kDa PEI. At this PEI molecular weight, the $\phi = 91\%$ sample recovers elastically from compression when cross-linked in the frozen state but is brittle to compression in the lyophilized analogue. For the $\phi = 67$ and 50% samples, monoliths prepared using both protocols recover elastically after compression. Both hydrated and lyophilized monoliths were prepared and data were collected at a frame rate of 1/s for 10 min. Wavelet-filtered particle trajectories were obtained (Supporting Information Figure S12) and used to obtain the van Hove distribution, viz., the distribution of particle jump distances in a time interval of 1 s. For each sample, data were obtained from fluorescent probe particles from several different spatial locations. The van Hove distribution is fitted well by a Gaussian whose width represents the diffusivity of the probe particle (Figure 4). For the $\phi = 91\%$ monoliths, diffusivities at different spatial locations in the

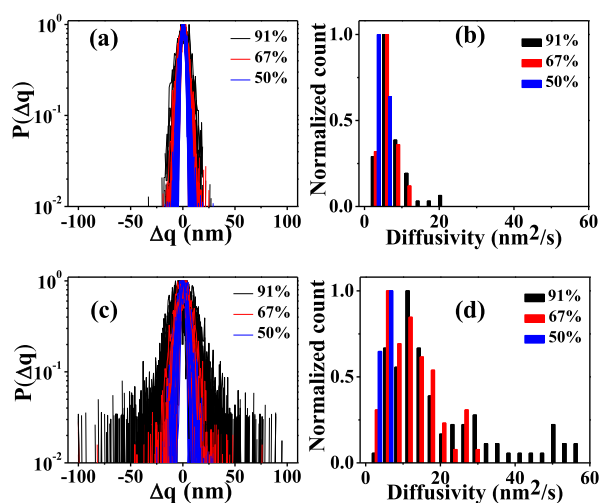


Figure 4. van Hove particle jump distribution for fluorescent probe particles embedded in the walls of hybrid monoliths cross-linked (a) in the presence of ice and (c) after lyophilization. Diffusivity values obtained from the variance of a Gaussian fit to the jump distributions in (a,c) are presented in (b,d), respectively. Data are presented for monoliths with $\phi = 91, 67,$ and 50% .

sample are narrowly distributed for the monolith cross-linked in the frozen state, relative to the lyophilized and cross-linked sample (compare Figure 4b,d). Thus, the lyophilized sample is characterized by significantly greater spatial heterogeneity than the “elastic” monolith. With a decrease in ϕ to 67 and 50%, the distribution of diffusivities for the “elastic” monolith narrows modestly. In comparison, the distribution narrows dramatically for lyophilized monoliths, such that for $\phi = 50\%$, there is virtually no difference between the diffusivity distribution for the two protocols. Thus, with a decrease in ϕ for the lyophilized monoliths, there is increased spatial homogeneity that correlates with the transition from brittle failure to elastic recovery. We have previously shown that the measured diffusivity is related to the local cross-link density.³³ Therefore, our data indicate that for high ϕ ($=91\%$), the distribution of cross-links in the polymer mesh is far more spatially homogeneous in the “elastic” monoliths relative to the lyophilized. With a decrease in ϕ , the spatial variation in cross-link density decreases for both “elastic” and lyophilized monoliths.

DISCUSSION

Our goal here is to rationalize the results as a function of the preparation protocol and nanoparticle loading. What is the microstructural origin of the qualitative change in mechanical properties at a critical ϕ ? At high ϕ ($=91\%$, e.g.), the initial aqueous dispersion contains particles with PEI adsorbed on them and free polymer and cross-linker in solution. When the water freezes, we anticipate that polymer chains and NPs are expelled to the growing ice front.⁴² In this picture, when the ice crystals impinge, the particles are organized into walls with a random close-packed structure, with unadsorbed polymer entirely localized in the interstitial spaces between the particles. It is likely that the polymer chains are solvated in water and remain in a swollen conformation (Figure 5a,b). We estimate the concentration, c , of unadsorbed polymer within the particle

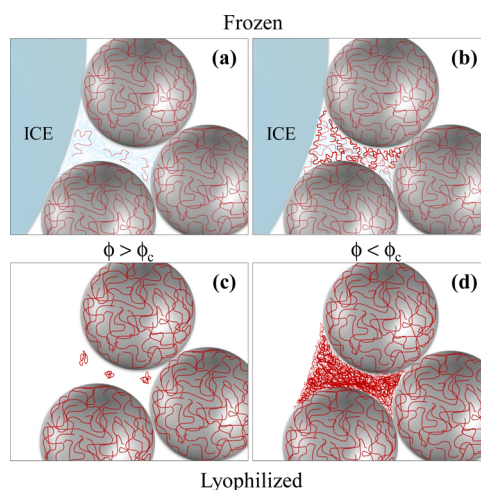


Figure 5. Proposed mechanism: (a,b) polymer chains in the frozen samples exhibit swollen conformation. Below a critical particle fraction (ϕ_c), swollen chains start overlapping each other and form a continuous network in the particle packing voids (b). However, for lyophilized samples, the removal of water by sublimation causes collapse of the chains (c). Below a critical particle fraction (ϕ_c), polymer chains in the particle packing voids form a melt phase (d). In melt state, polymer chains are shielded from bad solvent (air) even when the sample is lyophilized.

interstices and observe that $c \approx c^*$ corresponds to the critical ϕ_c for the elastic–brittle transition for the monolith (Supporting Information Figure S13 and Tables S1 and S2). The large spatial extent of the expanded chains results in more uniform cross-linking when c exceeds c^* when the polymers are cross-linked. This conclusion is consistent with the molecular weight-dependent study as shown in Figure 2, which shows that higher molecular weight polymers are more efficient in providing an elastic response; thus, the elastic behavior persists out to much higher solids loading, as expected by this chain conformation argument.

In contrast, when the sample is lyophilized, water is removed, resulting in collapse of the polymer chains that are now exposed to air, a bad solvent (Figure 5c). This results in a significant decrease in the spatial extent of the polymer chains and cross-linking happens in this state. At low polymer concentration, there are therefore large spatial heterogeneities in the distribution of cross-links. As ϕ decreases, there is a higher concentration of free chains resulting in an overlap in the coil volumes. At sufficiently high polymer concentrations, the polymer chains within the particle interstices form a melt phase (Figure 5d). The concentration of polymer segments in the melt phase is largely independent of the molecular weight—this is consistent with our result that the brittle–elastic transition for lyophilized samples happens at the same, ϕ_c , independent of PEI molecular weight. In the melt state, polymer chains are shielded from the bad solvent, air, even when the sample is lyophilized. These chains exist in a theta state and are cross-linked in this state. Therefore, the cross-link density is more spatially uniform for both “elastic” and lyophilized monoliths at these high-polymer concentrations. This argument is consistent with the fact that a much larger amount of polymer is required to obtain an elastic response from the cross-linked material in lyophilized state. The similarity in the critical ϕ at which a qualitative change is observed in the monolith mechanical response for the 22 nm and 1 μm monoliths strongly suggests that the transition in mechanical response is related to the infilling of interparticle voids by polymer.

The particle tracking measurements (Figure 4) and previous atomic force microscopy (AFM) studies³¹ indicate that the spatial heterogeneity in cross-link density in the polymer mesh is over length scales that are submicron to ~ 0 (1 μm). Below the critical particle loading ($\phi < \phi_c$), there is sufficiently high concentration of polymer chains that there is overlap everywhere in the interparticle regions where polymer is confined after freezing. When cross-linking is carried out under these conditions, there is spatially uniform, high cross-link density resulting in the formation of elastic monoliths. When $\phi > \phi_c$, then on average, the polymer concentration is below the overlap concentration (Figure 5). Statistical variations in the local polymer concentration result in large spatial variations in interchain cross-linking. This is manifested as spatial variation in work of adhesion (from AFM measurements³¹) and in tracer particle diffusion in microrheology. These variations are not at the length scale of a polymer coil, but at submicron to micron length scales.

Finally, why do we observe a decrease in modulus with increasing particle loadings, at high ϕ ? The modulus of the ice-templated hybrid monoliths is determined largely by cross-linked polymer mesh that envelops the particles. Therefore, the monoliths are soft, with moduli comparable to those of pure cross-linked polymer monoliths. Further, we have previously

demonstrated that the monolith modulus increases linearly with temperature, suggesting an entropic polymeric origin.²⁰ As ϕ decreases from 70 to 40%, the interparticle spacing varies from ≈ 23 to ≈ 29 nm. For a particle diameter of 22 nm, this corresponds to polymer chains confined to dimensions of a few nanometers. For the 25 kDa PEI chains, this confinement length scale is comparable to the polymer radius of gyration, R_g . It has been reported that confinement decreases the elastic moduli of ultrathin polymer films.^{43–45} We believe that an increase in polymer confinement for higher ϕ results in the observed modulus decrease.

CONCLUSIONS

Our results demonstrate the critical role of processing in determining the macroscopic mechanical properties of polymer nanocomposites. We ice-template porous polymer–particle hybrid nanocomposites comprising primarily of the particle phase with a small fraction of polymeric binder. The NP structure that results from both processing protocols is essentially the same—therefore, it is especially surprising that subtle variations in the processing protocols result in such dramatic differences in mechanical properties. We note that the mechanical properties of the nanocomposite hybrids exhibit moduli values comparable to the pure polymer network result even in the limit of very high NP loading—therefore, their mechanical response is determined by the cross-linked polymer phase that serves as a binder. Thus, we conjecture that the large differences in properties observed must arise not from the NP organization but must originate from the polymeric phase. Here, we show that these differences arise because polymer conformations, which are critical to the cross-linking and percolation of a polymer network, are centrally affected by solvent quality, polymer concentration, and molecular weight. In particular, the existence of overlapping polymer chains is critical to the creation of a percolated polymer network, and this threshold is sensitively determined by the variables discussed above. When the polymer chains are well solvated, high-molecular-weight polymers overlap at relatively low concentrations—therefore, monoliths prepared by cross-linking the polymer in the presence of ice are elastic at high NP loadings. However, at even higher NP loading, the polymer phase loses connectivity and then the material becomes brittle. In contrast, when the polymer is cross-linked after the monolith is lyophilized, substantially higher melt-like concentrations of polymer are required for samples that can recover after compression. Thus, the processing protocol critically determines the chain conformations in the (minority) polymer phase during nanocomposite preparation, thus controlling the mechanical properties.

ASSOCIATED CONTENT

Supporting Information

The Supporting Information is available free of charge on the ACS Publications website at DOI: 10.1021/acs.macromol.9b00813.

Mechanical response of ice-templated monoliths comprising 22 nm and 1 μm silica particles; SEM structure of the samples; SAXS on monoliths comprising 22 nm silica particles as are particle tracking data on samples containing fluorescent probe particles; and intrinsic viscosity measurements to determine the molecular

weight-dependent overlap concentration of PEI in water (PDF)

AUTHOR INFORMATION

Corresponding Authors

*E-mail: sk2794@columbia.edu. Phone: +1347 351-5314. Fax: +1 212 854-3054 (S.K.K.).

*E-mail: g.kumaraswamy@ncl.res.in. Phone: +91-20-2590-2182. Fax: +91-20-2590-2618 (G.K.).

ORCID

Karthika Suresh: 0000-0003-4890-2778

Arindam Chowdhury: 0000-0001-8178-1061

Sanat K. Kumar: 0000-0002-6690-2221

Guruswamy Kumaraswamy: 0000-0001-9442-0775

Notes

The authors declare no competing financial interest.

ACKNOWLEDGMENTS

K.S. thanks CSIR for the GATE fellowship. K.S. acknowledges Ramya Chulliyil for help with epifluorescence microscopy. K.S. also acknowledges Prashant Yadav for help with lyophilization. This work was partially supported through a grant from the BRNS, DAE, Government of India, and the IUSSTF Joint Center on Engineering Applications of Designer Nanoparticle Assemblies.

REFERENCES

- (1) Zhao, D.; Di Nicola, M.; Khani, M. M.; Jestin, J.; Benicewicz, B. C.; Kumar, S. K. Role of block copolymer adsorption versus bimodal grafting on nanoparticle self-assembly in polymer nanocomposites. *Soft Matter* **2016**, *12*, 7241–7247.
- (2) Maillard, D.; Kumar, S. K.; Fragneaud, B.; Kysar, J. W.; Rungta, A.; Benicewicz, B. C.; Deng, H.; Brinson, L. C.; Douglas, J. F. Mechanical properties of thin glassy polymer films filled with spherical polymer-grafted nanoparticles. *Nano Lett.* **2012**, *12*, 3909–3914.
- (3) Martin, T. B.; Seifpour, A.; Jayaraman, A. Assembly of copolymer functionalized nanoparticles: A Monte Carlo simulation study. *Soft Matter* **2011**, *7*, 5952–5964.
- (4) Jouault, N.; Vallat, P.; Dalmas, F.; Said, S.; Jestin, J.; Boué, F. Well-dispersed fractal aggregates as filler in polymer-silica nanocomposites: Long-range effects in rheology. *Macromolecules* **2009**, *42*, 2031–2040.
- (5) Krishnamoorti, R. Strategies for dispersing nanoparticles in polymers. *MRS Bull.* **2007**, *32*, 341–347.
- (6) Mackay, M. E.; Tuteja, A.; Duxbury, P. M.; Hawker, C. J.; Van Horn, B.; Guan, Z.; Chen, G.; Krishnan, R. S. General strategies for nanoparticle dispersion. *Science* **2006**, *311*, 1740–1743.
- (7) Corbierre, M. K.; Cameron, N. S.; Sutton, M.; Laaziri, K.; Lennox, R. B. Gold nanoparticle/polymer nanocomposites: Dispersion of nanoparticles as a function of capping agent molecular weight and grafting density. *Langmuir* **2005**, *21*, 6063–6072.
- (8) Mitchell, C. A.; Bahr, J. L.; Arepalli, S.; Tour, J. M.; Krishnamoorti, R. Dispersion of functionalized carbon nanotubes in polystyrene. *Macromolecules* **2002**, *35*, 8825–8830.
- (9) Kumar, S. K.; Ganesan, V.; Riggleman, R. A. Perspective: Outstanding theoretical questions in polymer-nanoparticle hybrids. *J. Chem. Phys.* **2017**, *147*, 020901.
- (10) Kumar, S. K.; Benicewicz, B. C.; Vaia, R. A.; Winey, K. I. 50th anniversary perspective: Are polymer nanocomposites practical for applications? *Macromolecules* **2017**, *50*, 714–731.
- (11) Kumar, S. K.; Krishnamoorti, R. Nanocomposites: Structure, phase behavior, and properties. *Annu. Rev. Chem. Biomol. Eng.* **2010**, *1*, 37–58.

(12) Harton, S. E.; Kumar, S. K. Mean-field theoretical analysis of brush-coated nanoparticle dispersion in polymer matrices. *J. Polym. Sci., Part B: Polym. Phys.* **2008**, *46*, 351–358.

(13) Akcora, P.; Liu, H.; Kumar, S. K.; Moll, J.; Li, Y.; Benicewicz, B. C.; Schadler, L. S.; Acehan, D.; Panagiotopoulos, A. Z.; Pryamitsyn, V.; Ganesan, V.; Ilavsky, J.; Thiagarajan, P.; Colby, R. H.; Douglas, J. F. Anisotropic particle self-assembly in polymer nanocomposites. *Nat. Mater.* **2009**, *8*, 354–359.

(14) Kumar, S. K.; Jouault, N.; Benicewicz, B.; Neely, T. Nanocomposites with polymer grafted nanoparticles. *Macromolecules* **2013**, *46*, 3199–3214.

(15) Akcora, P.; Kumar, S. K.; Moll, J.; Lewis, S.; Schadler, L. S.; Li, Y.; Benicewicz, B. C.; Sandy, A.; Narayanan, S.; Ilavsky, J. Gel-like mechanical reinforcement in polymer nanocomposite melts. *Macromolecules* **2009**, *43*, 1003–1010.

(16) Jouault, N.; Zhao, D.; Kumar, S. K. Role of casting solvent on nanoparticle dispersion in polymer nanocomposites. *Macromolecules* **2014**, *47*, 5246–5255.

(17) Wang, J.; Cheng, Q.; Tang, Z. Layered nanocomposites inspired by the structure and mechanical properties of nacre. *Chem. Soc. Rev.* **2012**, *41*, 1111–1129.

(18) Finnemore, A.; Cunha, P.; Shean, T.; Vignolini, S.; Guldin, S.; Oyen, M.; Steiner, U. Biomimetic layer-by-layer assembly of artificial nacre. *Nat. Commun.* **2012**, *3*, 966.

(19) Sellinger, A.; Weiss, P. M.; Nguyen, A.; Lu, Y.; Assink, R. A.; Gong, W.; Brinker, C. J. Continuous self-assembly of organic-inorganic nanocomposite coatings that mimic nacre. *Nature* **1998**, *394*, 256.

(20) Rajamanickam, R.; Kumari, S.; Kumar, D.; Ghosh, S.; Kim, J. C.; Tae, G.; Sen Gupta, S.; Kumaraswamy, G. Soft colloidal scaffolds capable of elastic recovery after large compressive strains. *Chem. Mater.* **2014**, *26*, 5161–5168.

(21) Deville, S., *Freezing Colloids: Observations, Principles, Control, and Use: Applications in Materials Science, Life Science, Earth Science, Food Science, and Engineering*; Springer, 2017.

(22) Wang, H.; Liu, H.; Wang, S.; Li, L.; Liu, X. Influence of tunable pore size on photocatalytic and photoelectrochemical performances of hierarchical porous TiO₂/C nanocomposites synthesized via dual-templating. *Appl. Catal., B* **2018**, *224*, 341–349.

(23) Wang, H.; Liu, X.; Wang, S.; Li, L. Dual templating fabrication of hierarchical porous three-dimensional ZnO/carbon nanocomposites for enhanced photocatalytic and photoelectrochemical activity. *Appl. Catal., B* **2018**, *222*, 209–218.

(24) Xu, T.; Liu, X.; Wang, S.; Li, L. Ferroelectric Oxide Nanocomposites with Trimodal Pore Structure for High Photocatalytic Performance. *Nano-Micro Lett.* **2019**, *11*, 37.

(25) Xu, T.; Wang, S.; Li, L.; Liu, X. Dual templated synthesis of trimodal porous SrTiO₃/TiO₂@ carbon composites with enhanced photocatalytic activity. *Appl. Catal., A* **2019**, *575*, 132–141.

(26) Estevez, L.; Kelarakis, A.; Gong, Q.; Da'as, E. H.; Giannelis, E. P. Multifunctional graphene/platinum/nafion hybrids via ice templating. *J. Am. Chem. Soc.* **2011**, *133*, 6122–6125.

(27) Chatterjee, S.; Shanmuganathan, K.; Kumaraswamy, G. Fire-retardant, self-extinguishing inorganic/polymer composite memory foams. *ACS Appl. Mater. Interfaces* **2017**, *9*, 44864–44872.

(28) Das, C.; Chatterjee, S.; Kumaraswamy, G.; Krishnamoorthy, K. Elastic compressible energy storage devices from ICE templated polymer gels treated with polyphenols. *J. Phys. Chem. C* **2017**, *121*, 3270–3278.

(29) Chatterjee, S.; Sen Gupta, S.; Kumaraswamy, G. Omniphilic polymeric sponges by ice templating. *Chem. Mater.* **2016**, *28*, 1823–1831.

(30) Chatterjee, S.; Potdar, A.; Kuhn, S.; Kumaraswamy, G. Preparation of macroporous scaffolds with holes in pore walls and pressure driven flows through them. *RSC Adv.* **2018**, *8*, 24731–24739.

(31) Suresh, K.; Patil, S.; Rajamohanam, P. R.; Kumaraswamy, G. The Template Determines Whether Chemically Identical Nanoparticle Scaffolds Show Elastic Recovery or Plastic Failure. *Langmuir* **2016**, *32*, 11623–11630.

(32) Suresh, K. Structure and Properties of Ice Templated Macroporous Particle-Polymer Hybrid Assemblies. Ph.D. Dissertation, CSIR-National Chemical Laboratory, Pune, India, 2018.

(33) Suresh, K.; Sharma, D. K.; Chulliyil, R.; Sarode, K. D.; Kumar, V. R.; Chowdhury, A.; Kumaraswamy, G. Single-Particle Tracking To Probe the Local Environment in Ice-Templated Crosslinked Colloidal Assemblies. *Langmuir* **2018**, *34*, 4603–4613.

(34) Kohlbrecher, J. *SASfit: A Program for Fitting Simple Structural Models to Small Angle Scattering Data*; Paul Scherrer Institut, Laboratory for Neutron Scattering, 2008.

(35) Bhattacharya, S.; Sharma, D. K.; Saurabh, S.; De, S.; Sain, A.; Nandi, A.; Chowdhury, A. Plasticization of poly (vinylpyrrolidone) thin films under ambient humidity: Insight from single-molecule tracer diffusion dynamics. *J. Phys. Chem. B* **2013**, *117*, 7771–7782.

(36) Guth, E. Theory of filler reinforcement. *J. Appl. Phys.* **1945**, *16*, 20–25.

(37) Kumari, S.; Kulkarni, A.; Kumaraswamy, G.; Sen Gupta, S. Large Centimeter-Sized Macroporous Ferritin Gels as Versatile Nanoreactors. *Chem. Mater.* **2013**, *25*, 4813–4819.

(38) Torquato, S.; Truskett, T. M.; Debenedetti, P. G. Is random close packing of spheres well defined? *Phys. Rev. Lett.* **2000**, *84*, 2064.

(39) Borkovec, M.; Papastavrou, G. Interactions between solid surfaces with adsorbed polyelectrolytes of opposite charge. *Curr. Opin. Colloid Interface Sci.* **2008**, *13*, 429–437.

(40) Mészáros, R.; Varga, I.; Gilányi, T. Adsorption of poly (ethyleneimine) on silica surfaces: Effect of pH on the reversibility of adsorption. *Langmuir* **2004**, *20*, 5026–5029.

(41) Suresh, K.; Kumaraswamy, G. Effect of Electrostatic Interactions on Structure and Mechanical Properties of Ice Templated Colloid-Polymer Composites. *J. Phys. D: Appl. Phys.* **2019**, *52*, 214002.

(42) Deville, S.; Maire, E.; Bernard-Granger, G.; Lasalle, A.; Bogner, A.; Gauthier, C.; Leloup, J.; Guizard, C. Metastable and unstable cellular solidification of colloidal suspensions. *Nat. Mater.* **2009**, *8*, 966.

(43) Stafford, C. M.; Vogt, B. D.; Harrison, C.; Julthongpipit, D.; Huang, R. Elastic moduli of ultrathin amorphous polymer films. *Macromolecules* **2006**, *39*, 5095–5099.

(44) Crosby, A. J.; Lee, J. Y. Polymer nanocomposites: The “nano” effect on mechanical properties. *Polym. Rev.* **2007**, *47*, 217–229.

(45) Torres, J. M.; Stafford, C. M.; Vogt, B. D. Manipulation of the elastic modulus of polymers at the nanoscale: Influence of UV- ozone cross-linking and plasticizer. *ACS Nano* **2010**, *4*, 5357–5365.